Mars precession rate determined from radiometric tracking of the InSight Lander

Daniel S. Kahan [a,*], William M. Folkner [a], Dustin R. Buccino [a], Véronique Dehant [b],
Sébastien Le Maistre [b], Attilio Rivoldini [b], Tim Van Hoolst [b], Marie Yseboodt [b], J.C. Marty [c]

[a] *Jet Propulsion Laboratory, 4800 Oak Grove Dr., Pasadena, CA, 91109, USA*
[b] *Royal Observatory of Belgium, av. Circulaire 3, B1180, Brussels, Belgium*
[c] *CNES/GRGS, OMP 14 avenue Edouard Belin, 31400, Toulouse, France*

ABSTRACT

The Interior Exploration using Seismic Investigations, Geodesy, and Heat Transport (InSight) mission has provided an opportunity to improve our knowledge of Mars' interior via the Rotation and Interior Structure Experiment (RISE). RISE provides information on the rotation of Mars by measuring the Doppler shift of radio transmissions from InSight to NASA's Deep Space Network (DSN) on Earth. Through the combination of one year of Doppler data from InSight with previous data from the Viking-1 lander, Mars Pathfinder, and Opportunity missions, data spanning 43 years from 1976 to 2019 are used to estimate the Mars precession rate as −7605 ± 3 milliarcseconds per year. This result is consistent with the precession rate estimated from Doppler tracking of previous landers and orbiters alone.

1. Introduction

Landing on Mars on November 26, 2018, the Interior Exploration using Seismic Investigations, Geodesy, and Heat Transport (InSight) mission communicates with Earth via relays with Mars orbiters and by direct radio transmissions to and from NASA's Deep Space Network (DSN). InSight's Rotation and Interior Structure Experiment (RISE) makes use of the InSight/DSN transmissions by measuring the range rate of the round-trip signal, which is proportional to the velocity of the lander along the line of sight (LOS) with respect to Earth. These Doppler measurements provide information on the rotation of Mars (e.g., Folkner et al., 1997; Kuchynka et al., 2014). This paper discusses the methodology for determination of the Mars precession rate based on data collected during the first year of the InSight mission along with previous measurements from the Viking-1 lander, Pathfinder, and Mars Exploration Rover Opportunity. An updated computation of that value is provided along with a computation of Moment of Inertia (MOI) based on recently estimated parameters such as the degree-2 order-0 gravity field J_2.

The precession of Mars' axis of rotation is caused by the Sun's gravitational pull on the equator of the Mars ellipsoid as it rotates. It takes approximately 170,000 years for the spin axis to rotate once about the normal to the orbit plane, while nutations of the rotation axis occur on a period of 1 Martian year or less due to the relative Mars-Sun orientation as well as to the gravitational torques of Phobos and Deimos (Reasenberg and King, 1979; Baland et al., 2020). The MOI determined from the precession rate can help determine interior properties of Mars (Folkner et al., 1997). Additionally, together with the degree-two gravity field, the precession rate determines Mars' global moment of inertia, which is a key element for the calculation of obliquity and insolation history and therefore also for the modeling of the Martian climate over millions of years (Bouquillon, 2000; Ward, 1974; Laskar, 1988; Tourma and Wisdom, 1993; Francois et al., 1990). The data set is not yet long enough to separate the nutation contributions from precession or obliquity rates. The nutations during the InSight time frame are taken into account but fixed to the values from a rigid Mars model (Reasenberg and King, 1979; Baland et al., 2020).

Measurement of the radio range from communications with the Viking landers provided the first estimation of Mars' precession from landers on Mars (Yoder and Standish, 1997). For those missions, there was no programmatic impetus for the archival of tracking data; however,
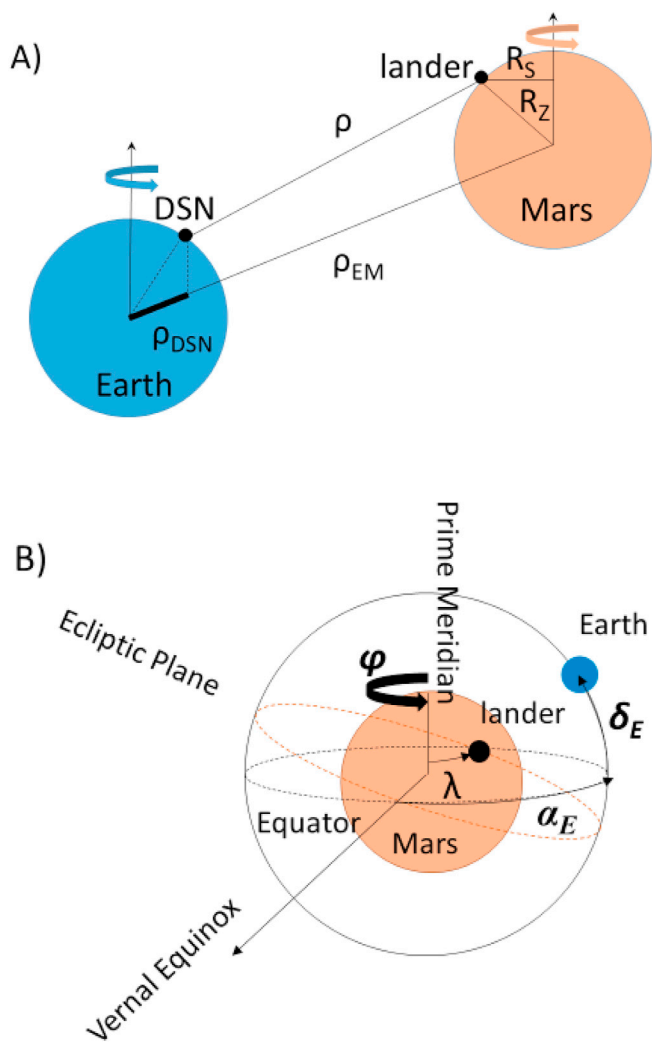
Fig. 1. Geometry for computation of the Doppler shift of a landed asset on Mars.

two years of Doppler measurements from Viking-1 were recovered (a small amount of Viking-2 data were recovered but are not employed in this study). Those two years of data from Viking-1 were later combined with data from Mars Pathfinder, yielding an observed precession of -7576 ± 35 milliarcseconds per year (Folkner et al., 1997). In 2014, Kuchynka et al. combined 4 months of tracking data from a stationary period of the Opportunity rover with the Viking-1 and Pathfinder data to improve the landers/rover precession estimate to -7619.5 ± 6.4 mas/yr. Doppler tracking data of the same landers plus spacecraft in orbit about Mars (Mars Global Surveyor, Mars Odyssey, and Mars Reconnaissance Orbiter) have also been used to estimate the Martian precession rate,

with a most recent estimate of -7608.3 ± 2.1 mas/yr (Konopliv et al., 2016).

This study builds upon the work of Kuchynka et al. (2014) by adding one year of data from the recently landed InSight mission. The large displacement of the Martian pole between missions allows for more accurate determination of the linear drift of the pole. Now spanning 43 years from 1976 to 2019, the combined data set yields updated constraints on the mean precession rate and other rotation parameters. Section 2 of this paper describes the nature and source of the measurements involved; Section 3 discusses the treatment of range-rate noise; Section 4 discusses the analysis of the data; Section 5 interprets the results; and Section 6 provides conclusions.

2. Measurements

The measurements in this analysis are the range rates of the radio signals transmitted from the DSN to the lander and phase coherently transmitted back to the DSN on Earth. The measured Doppler shift approximates the rate of change of distance ρ along the LOS between the tracking station and the lander. Yoder and Standish (1997) provide a description of the range rate as:

$$\frac{\partial \rho}{\partial t} = \frac{\partial \rho_{EM}}{\partial t} + \frac{\partial \rho_{DSN}}{\partial t} - \frac{\partial}{\partial t}[R_z \sin\delta_E + R_S \cos\delta_E \cos(\phi + \lambda - \alpha_E)] \quad (1)$$

where ρ_{EM} is the Earth-Mars distance, ρ_{DSN} is the norm of the component of the center of Earth to DSN antenna vector projected to the Earth-Mars direction, R_z is the distance of the lander from the Martian equatorial plane (geocentric elevation), R_S is the distance from the Martian spin axis to the lander (geocentric latitude), ϕ is the angle of rotation of Mars about its spin axis (between the prime meridian direction at t and its direction at the J2000 reference epoch), λ is the lander longitude, α_E is the right ascension (the angle in the Martian equatorial plane measured from where the Sun crosses that plane from south to north [Martian vernal equinox]), and δ_E is the declination (the angle from the Martian mean equatorial plane) of Earth as viewed from Mars. See Fig. 1.

The direction of Mars' spin axis, and therefore precession, can be gleaned through changes in the Earth declination δ_E and right ascension α_E observed via the Doppler measurements. These changes impact the amplitude and phase of the diurnal effect in the last term of Equation (1). For example, when Earth declination approaches zero, the Mars rotation axis nears perpendicularity to the LOS, lessening this signature (Yseboodt et al., 2017).

To estimate Mars' precession, the InSight tracking data covering November 27, 2018, to November 30, 2019, are joined with previous data from the Viking-1 lander, encompassing over 1 Martian year from 1976 to 1979, from Mars Pathfinder, covering roughly 90 days in 1997, and from Opportunity, which was stationary for four months in 2012. Table 1 summarizes the lander data sets. A brief description of the parameters for each mission follows, along with a summary of the calibrations applied to account for the tropospheres and ionospheres of Earth and Mars.

Table 1
Lander/rover tracking data at 60-s integration time considered in this study. The estimated accuracy corresponds to the root mean square of the frequency residuals determined in a fit of the model.

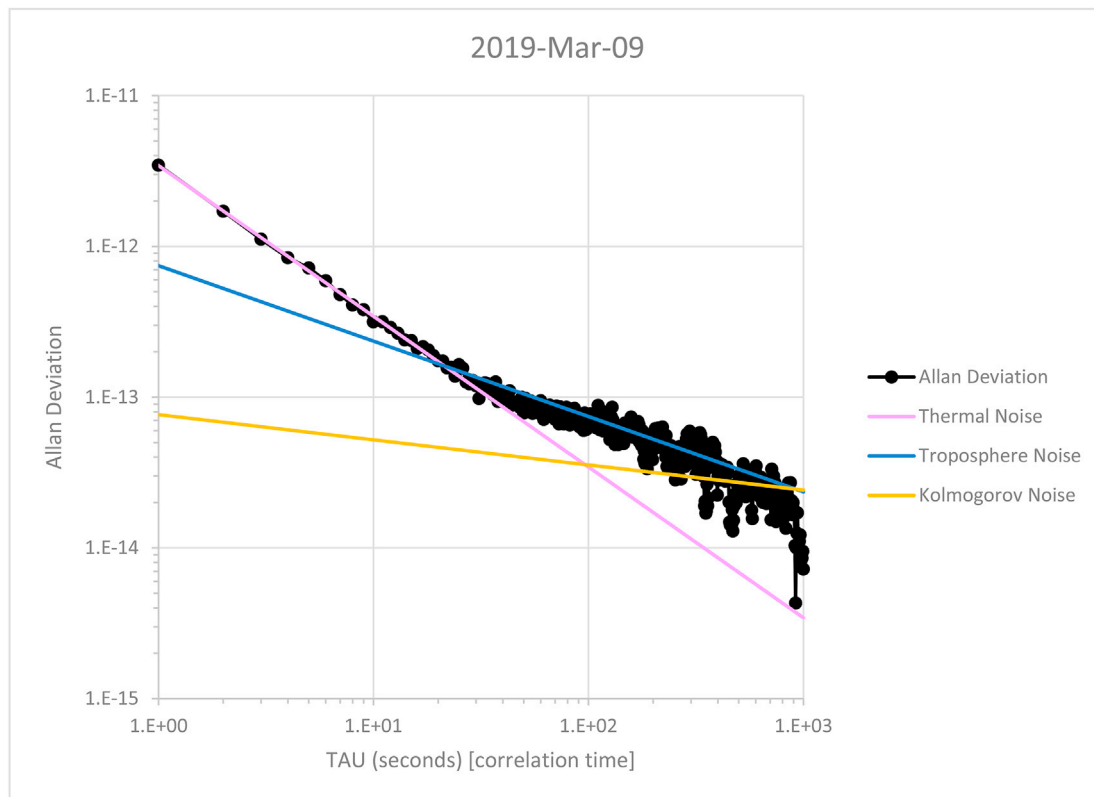|	Number of Passes	Mean Pass Duration (minutes)	Number of Data Points	Time Range	Sun-Earth-Probe Angles (degrees)	Approximate Accuracy (mm/s)
Viking 1	208	73	15230	21-Jul-1976 to 20-Dec-1978	1 to 176	0.42
Pathfinder	107	75	7995	04-Jul-1997 to 25-Sep-1997	55 to 85	0.037
Opportunity	59	23	1373	10-Jan-2012 to 04-May-2012	110 to 176	0.017
InSight	241	49	11755	27-Nov-2018 to 30-Nov-2019	2 to 92	0.037

Fig. 2. Allan Deviation versus correlation time (TAU) based on Doppler residuals over a tracking pass.

2.1. Viking

The first of the two-part Viking mission, Viking-1 was the first spacecraft to successfully land and operate from the surface of Mars. The mission consisted of both an orbiter and a lander, and the lander was designed to take high-resolution images and study the surface and atmosphere of Mars. The Viking-1 lander landed in Chryse Planitia (22.49°N, 48.04°W) on July 20, 1976, and the mission lasted until November 11, 1982 (Viking Mission to Mars, 1988).

The Viking-1 lander communicated with its orbiter through an ultra-high frequency (UHF) relay system and directly with Earth via an S-Band communication system (2.1 GHz uplink, 2.3 GHz downlink). The S-Band system consisted of two receivers, one using a low gain antenna (LGA) to receive commands from Earth and one using a high gain antenna (HGA). The HGA, a 76-cm diameter parabolic reflector dish, was steerable and could be pointed directly at Earth (Soffen and Snyder, 1976). Over two years of S-Band Doppler data, while Viking-1 was transmitting with the HGA, were retrieved by Folkner et al. (1997) and are similarly used in this study (neither Viking-1 nor Viking-2 Doppler data were archived). The data used in the fitting process consist of 15,230 60-s data points over 208 passes between July 21, 1976, and December 20, 1978 (Table 1).

2.2. Pathfinder

The Mars Pathfinder mission was the first mission to deliver a wheeled rover (Sojourner) to another planet. Pathfinder landed in Ares Vallis (19.17°N, 33.21°W) on July 4, 1997 (Golombek et al., 1997), and the mission lasted until September 27, 1997.

Similar to Viking, Pathfinder's radio system included a LGA and a steerable HGA (Golombek, 1997). While the Sojourner rover communicated directly with the base station (formally named the Carl Sagan Memorial Station after landing), this station communicated with Earth via its X-Band communication system (7.2 GHz uplink, 8.4 GHz downlink). Radio tracking of Pathfinder was used to attain a precise measure of Mars' pole of rotation, constraining the radius of the planet's core to between 1300 and 2000 km (Golombek et al., 1997).

The Pathfinder data contribute 7995 60-s data points over 107 passes from July 4, 1997, to September 25, 1997, to the fitting process (Table 1). Although the span of the Pathfinder data is relatively short, the combination with the Viking data shows the motion of the Martian pole due to precession over a period of twenty years (Folkner et al., 1997).

2.3. Opportunity

On January 24, 2004, the Mars Exploration Rover Opportunity landed in Eagle crater on Meridiani Planum (2.2°S, 5.4°W), 21 days after the landing of Spirit at Gusev crater. The primary mission of both rovers was to explore locations on the Martian surface where water may have once been present and to assess past environmental conditions and their capability to support life (Squyres et al., 2004). Opportunity continued operations until June 2018 when it was engulfed by a planet-wide dust storm and lost communications with Earth. Although both rovers were in transit most of the time, between January and May 2012 Opportunity remained in one spot, saving energy during Martian winter. During that time, the MER Radio Science Tracking Experiment (Kuchynka et al., 2014) was conducted by the DSN, with the express purpose of collecting additional Doppler data for improved calculation of Mars rotation parameters.

Similar to Pathfinder, Opportunity transmitted at X-Band and had both a LGA and a steerable HGA. The HGA was used for the bulk of the experiment, with approximately 20 tracks of durations less than 5 min acquired on the LGA. Because the HGA passes occurred with Earth at a more sensitive geometry (lower elevation angles), and because they tended to be longer (up to 30 min) (Kuchynka et al., 2014), they are the only ones used in this study.

The Opportunity 60-s data applied in this study from the MER Radio Science Tracking Experiment consist of 1373 points over 59 passes
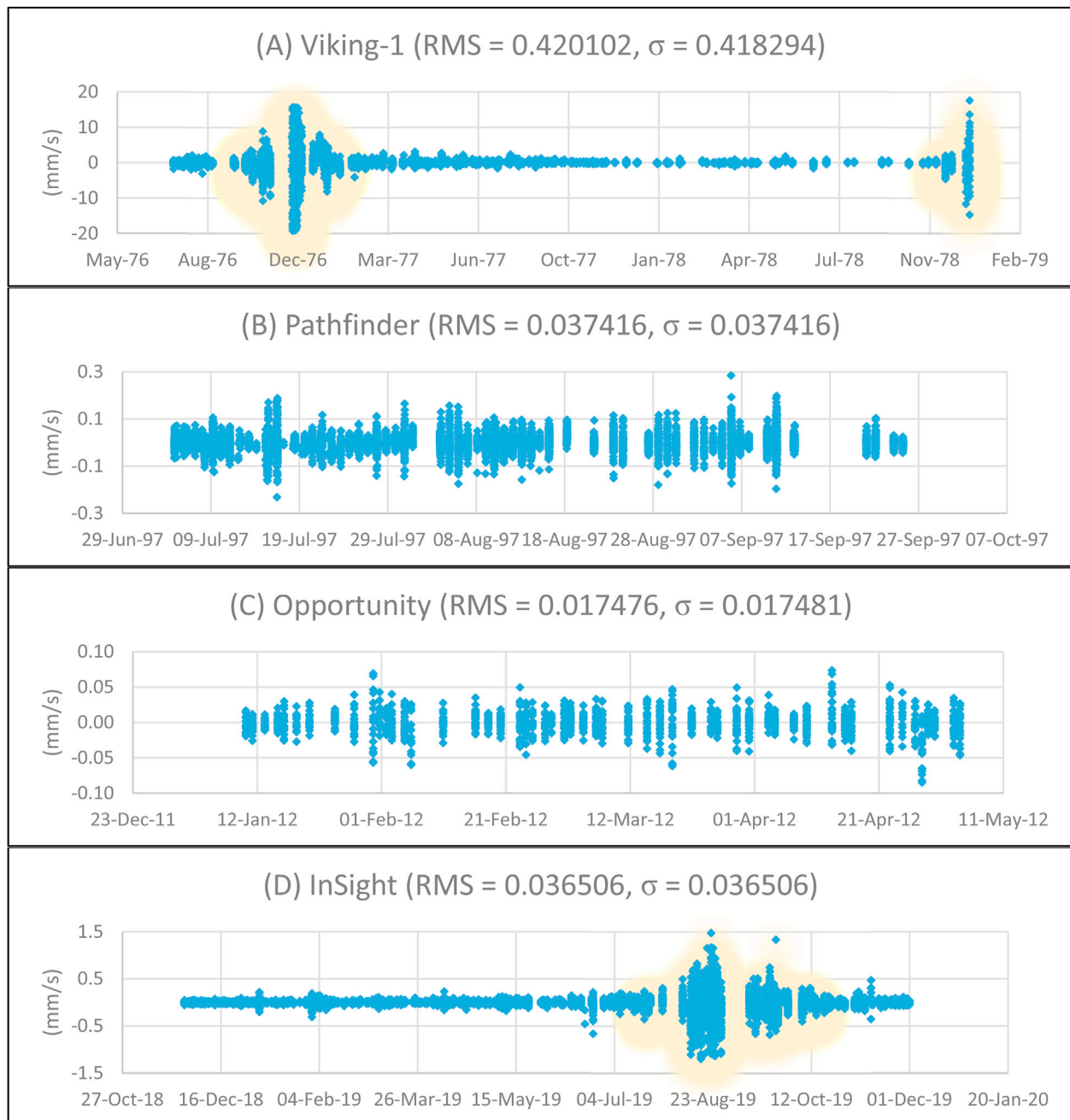
Fig. 3. Frequency residuals, root mean square error (RMS), and standard deviation (σ) in millimeters per second for (A) Viking-1 (July 21, 1976, to December 20, 1978); (B) Pathfinder (July 4, 1997, to September 25, 1997); (C) Opportunity (January 2, 2012, to May 4, 2012); (D) Insight (November 27, 2018, to November 30, 2019) based on a model fit for all four landers. Shaded regions indicate SEP angle <15° (not included in computation of RMS or σ).

acquired between January 10, 2012, and May 4, 2012 (Table 1). The addition of Doppler data from the MER Radio Science Tracking Experiment to the Viking and Pathfinder sets increased the range of direct radiometric tracking of the Martian surface from about 20 years to more than 35 years, and the updated precession rate based on these three missions is discussed by Kuchynka et al. (2014).

2.4. InSight

InSight landed as intended in Elysium Planitia on Mars (4.50°N, 135.62°E) on November 26, 2018 (Golombek et al., 2020), and has recently completed its primary science phase as of December 2020. A thermally controlled enclosure below the lander's main platform contains the lander's Small Deep-Space Transponder (SDST) and solid-state

power amplifier (SSPA). As with Pathfinder and Opportunity, an X-Band (7.2 GHz) carrier signal is sent from a DSN antenna, received by the SDST, amplified by the SSPA, and phase coherently transmitted back to Earth (at 8.4 GHz) to the same DSN antenna (with a turnaround ratio of 880/749).

Unlike the other three missions, the SDST and SSPA for InSight RISE are linked to two fixed-pointing medium-gain antennas (MGAs), which are located on the main platform (Folkner et al., 2018). InSight azimuthal orientation was controlled during landing in order to ensure good viewing geometry for RISE via one antenna or the other, while also allowing commanding from Earth throughout the mission. One antenna points 5.06° northward from due west, and the other points 16.8° southward from due east. With this orientation, Earth is usually viewable when rising over the eastward antenna or when setting over the

Table 2

Mars rotation and orientation parameters adjusted to InSight, Opportunity, Pathfinder, and Viking-1 data. Uncertainties are 1-sigma uncertainty bounds.

| Mars Rotation Parameter	Value	Uncertainty
Mars orbit inclination of 1980 J (°)	24.67682669	Fixed
Longitude of Mars orbit ascending node of 1980 N (°)	3.37919183	Fixed
Rotation about pole ϕ (°)	133.3861997	0.00001
Rotation rate ω (°/day)	350.8919825	0.0000002
Longitude of node at J2000 ψ_0 (°)	81.9683988	0.000003
Precession rate $d\psi/dt$ (mas/yr)	−7605	3.0
Obliquity ε (°)	25.18938228	0.000001
Obliquity rate $d\varepsilon/dt$ (mas/yr)	−5.4	1
Annual term C1 in $\delta\phi$ (mas)	481	6
Semiannual term C2 in $\delta\phi$ (mas)	−117	5
Triannual term C3 in $\delta\phi$ (mas)	−19	4
Quarterly term C4 in $\delta\phi$ (mas)	−5	3.5
Annual term S1 in $\delta\phi$ (mas)	−144	6
Semiannual term S2 in $\delta\phi$ (mas)	−94	4.5
Triannual term S3 in $\delta\phi$ (mas)	−8	4.5
Quarterly term S4 in $\delta\phi$ (mas)	−3.5	4
InSight longitude (°)	135.6178	0.0003
InSight cylindrical radius (km)	3382.6129	0.0001
InSight z (km)	266.07	0.02
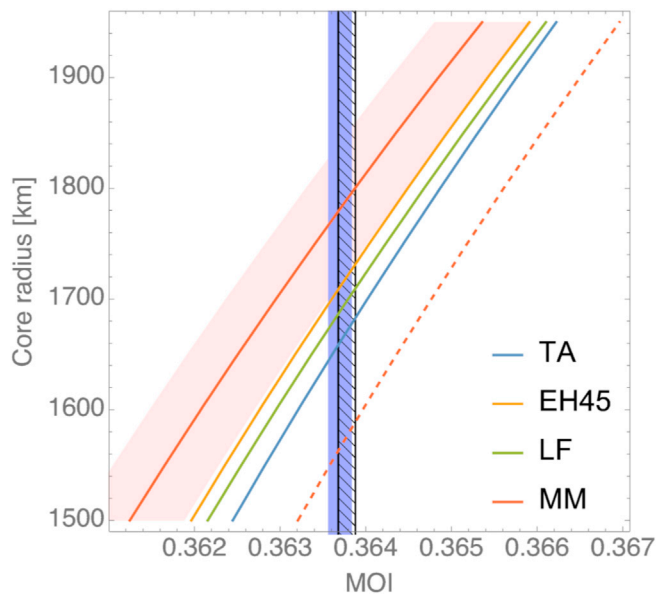
Fig. 4. Relation between core radius and normalized moment of inertia for a set of plausible Mars mantle compositions assuming a fixed crust density (ρ) and thickness (d) and mantle temperature (case 16, Plesa et al., 2016). The acronyms stand for the different mantle mineralogy models (TA: Taylor (2013), $d = 95$ km, $\rho = 2865$ kg/m^3; EH45: Sanloup et al. (1999), $d = 70$ km, $\rho = 2834$ kg/m^3; LF: Lodders and Fegley (1997), $d = 70$ km, $\rho = 2834$ kg/m^3; MM: Mohapatra and Murty (2003), $d = 65$ km, $\rho = 2826$ kg/m^3. The red shaded area indicates the effect of a crust thickness variation of ±10 km on the crust thickness of the MM models and the dashed red line illustrates the effect of the mantle temperature (case 22, Plesa et al., 2016) on the MM models. The hatched area indicates the normalized moment of inertia value (0.3637) at 1 sigma of Konopliv et al. (2016) and the blue shaded area represents the normalized MOI value of this study.

westward antenna; the typical amount of tracking time for one day is 30 min to an hour. The tilt at the landing site is 4° (Agle et al., 2018), well within the MGA patterns, which were designed to accommodate angles up to 15° (Golombek et al., 2017). Each MGA points 30° upwards from the platform's main deck (Folkner et al., 2018).

The InSight data set consists of 11,755 data points over 241 passes from November 27, 2018, to November 30, 2019, and provides a robust addition to the existing data from the previous three missions, extending

the data arc from 35 to 43 years. The location of InSight based on RISE estimates is 4.49751°N by 135.6178693°E (Golombek et al., 2020). Note that in this paper we formally distinguish between the two unique locations of the east and west antennas, which are separated by a constant 1.55 m.

2.5. Media calibrations

Radio waves bend as they travel through the atmosphere. The refractive index (the ratio of the propagation speed in a vacuum to the speed of propagation in another medium) in Earth's troposphere imparts a significant signature to the propagation of radio waves and thus to the Doppler data. This refractive index is mainly related to common atmospheric quantities of pressure and temperature. After calibration of the data, the noise due to remaining water vapor is the dominant component and tends to be greater during Earth's daylight hours when atmospheric warming increases water vapor capacity (Asmar et al., 2005). The contribution from the dry troposphere is of a larger amount but is well determined from the DSN local pressure and temperature reporting. Another effect, one tenth in scale to that of the troposphere, is caused by Earth's ionosphere. Most of the ionosphere is ionized due to the large amount of solar radiation, which increases the amount of free electrons during the day. As radio waves enter Earth's ionosphere from space, some of the waves are absorbed by the electrons in the ionosphere by an amount inversely proportional to the frequency of the waves. Signals from global positioning system satellites are recorded each day at the DSN and are used to calibrate these effects at X-band frequency (Bar-Sever et al., 2007; Mannucci et al., 1998).

The thin troposphere of Mars has its own small effect on the Doppler measurements, well below the noise caused by water vapor fluctuations on Earth, but comparable to Earth ionosphere noise. For this analysis, we calibrate tropospheric noise at Mars with a simple model provided by Le Maistre (2020). The delay caused by the Mars troposphere is defined as 5 cm divided by sin (E) where E is the elevation angle of Earth as viewed by the lander. Although the effects are negligible with respect to the Mars precession (<1 mas/yr), they are nonetheless applied in this analysis. In the coming months with additional data, this calibration may be essential for extracting the liquid core contribution in the nutation signal.

Approximately one fifth as noisy as the Martian troposphere, the Martian ionosphere also has a small effect on the Doppler data (Lillis et al., 2010; Bergeot et al., 2019). Because this amount is close to the level of the Doppler noise, the Martian ionosphere is not calibrated for this study. See Folkner et al. (2018) or Dehant et al. (2020) for other noise sources considered to be below the contribution from tropospheric water vapor which are disregarded for this study. There is however one exception, the plasma effects that can be quite high when the Sun-Earth-Probe (SEP) angle is close to zero (see below).

3. Doppler noise

Prior to analysis of the InSight data, the first step is to average the data over a convenient time interval in a way that properly accounts for the various noise sources. The DSN receiver records the Doppler shift every 0.1 s. At short integration times, the dominant noise source is thermal noise due to limited signal-to-noise ratio in the radio link (Armstrong, 1998). At longer integration times, the dominant noise source is phase scintillation caused by wave propagation through media, especially Earth's troposphere. Based upon the data collected so far for InSight, the average integration time where the transition from thermal noise to troposphere noise occurs is around 20 s (for example, see Fig. 2). Thus, the Doppler data have been integrated to give phase versus time and the resulting phase is averaged over 20 s. Differences in average phase divided by 20 s then gives Doppler data with negligible thermal noise. These Doppler data are then averaged over 60 s to reduce the noise from troposphere fluctuations. Thanks to their HGA steerable antennas, the previous three mission measurements had higher signal-to-noise ratio
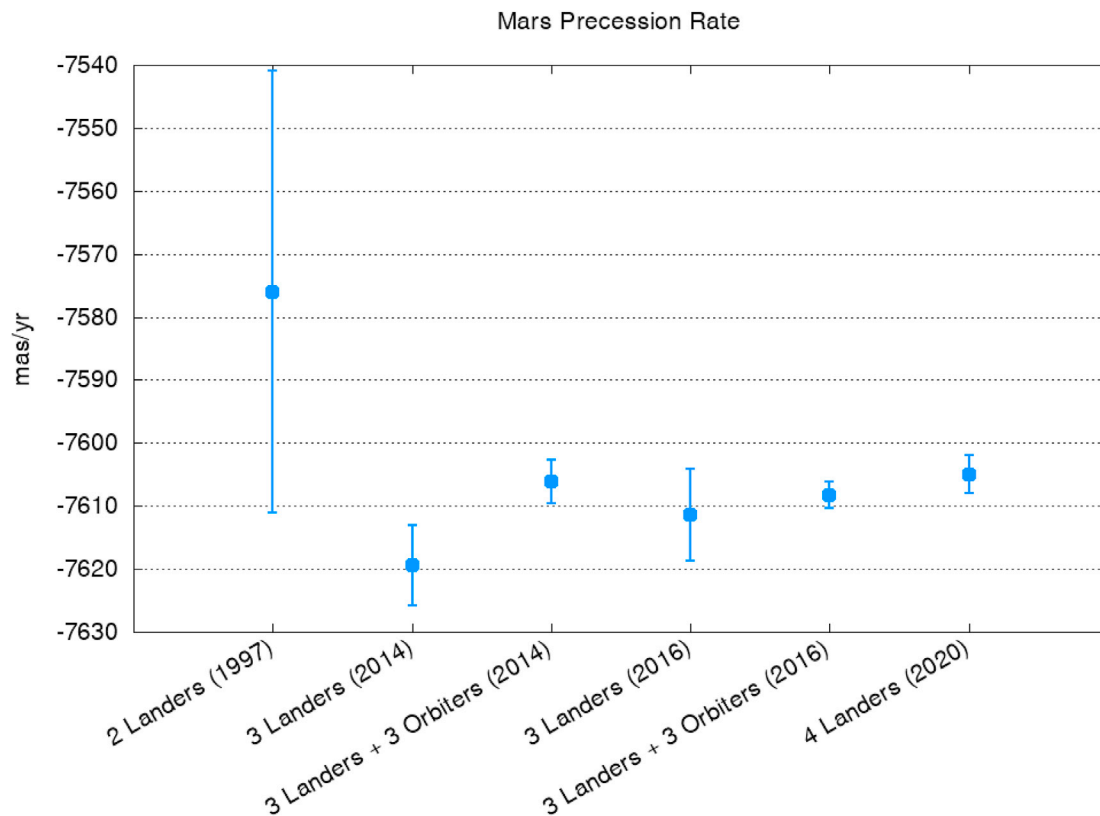
Mars Precession Rate

Fig. 5. Mars precession rate and 1-sigma uncertainty based on Viking-1 and Pathfinder ("2 Landers (1997)", Folkner et al., 1997); Viking-1, Pathfinder, and Opportunity ("3 Landers (2014)", Kuchynka et al., 2014); Viking-1, Pathfinder, Opportunity, Mars Global Surveyor orbiter, Odyssey orbiter, and Mars Reconnaissance Orbiter ("3 Landers + 3 Orbiters (2014)", Kuchynka et al., 2014); Viking-1, Pathfinder, and Opportunity ("3 Landers (2016)", Konopliv et al., 2016); Viking-1, Pathfinder, Opportunity, Mars Global Surveyor orbiter, Odyssey orbiter, and Mars Reconnaissance Orbiter ("3 Landers + 3 Orbiters (2016)", Konopliv et al., 2016); and Viking-1, Pathfinder, Opportunity, and InSight combined ("4 Landers (2020)").

than InSight, so the thermal noise was negligible and the 0.1-s Doppler data were directly averaged over 60 s. Both noise sources are considered white, having nearly Gaussian noise distributions. To fit Doppler data dominated by white noise, the data are weighted by the root-mean-square (RMS) of the residuals (the difference between the observed and expected Doppler shift).

In addition to the thermal and troposphere noise, the speed of radio propagation, and hence the Doppler measurement, is affected and sometimes dominated by phase scintillation from continual variations in the total electron content (solar plasma) between Mars and Earth. Because the amount of solar plasma is greatest near the Sun, closer position of the Mars-Earth ray path to the Sun (typically denoted as the SEP angle) is correlated with greater plasma noise. For Viking-1, because solar plasma noise is inversely proportional to the square of the radio frequency, the S-Band Doppler dataset is dominated by solar plasma noise, unlike the other landers that used X-band. The Pathfinder and Opportunity data noise were taken at large enough SEP angle so that the solar plasma noise was less than the troposphere noise. For InSight, most Doppler data noise was dominated by troposphere noise, except for ~90 days around September 2, 2019, (solar conjunction) when the data noise was dominated by solar plasma. We define the cut-off point at SEP = 15°, where the solar plasma noise is greater than the thermal noise, which happens between July 16th and Oct. 18th, 2019. During this period the noise becomes colored (Kolmogorov noise, see Folkner, 2017), meaning that subsequent data points become correlated, which is not suitable for proper application of the least-squares fitting method used by the orbit determination and analysis software. To account for charged particle content, Viking data and InSight data near solar conjunction are de-weighted from the RMS by a factor of 5.3 to account for the non-white

power spectral density of the solar plasma noise for estimation of signatures with near-diurnal frequency (see Appendix A).

4. Analysis

Once compressed, the 60-s tracking measurements from all four missions are analyzed to solve for Mars rotation using the Jet Propulsion Laboratory (JPL) Mission analysis, Operations and Navigation Toolkit Environment (MONTE) program (Evans et al., 2018) and the Center National d'Etudes Spatiales (CNES) Géodésie par Intégrations Numériques Simultanées (GINS) software (Marty et al., 2011), adapted and used by the Royal Observatory of Belgium (ROB) for planetary applications. Both programs are designed for orbital determination and trajectory optimization and analysis.

In order to compute the predicted Doppler (Eq. (1)) to be fitted to the measurements, both Earth and Mars antenna positions must be expressed in the same reference frame, chosen to be the Solar System Barycenter J2000 for the sake of simplicity. Conversion to J2000 from Mars-fixed coordinates is accomplished by modeling of rotation, precession and obliquity rate, and nutation about the spin axis (Konopliv, 2006). See Yoder and Standish (1997) and Sears and Brehme (1968) for discussion on the correction for relativistic effects. Rotation about the spin axis is expressed by angle ϕ (from Eq. (1)) and variations $\delta\phi$ developed as a sum of four harmonics

$$\delta\phi = \sum_{j=1}^{4} \left(C_j \cos jl + S_j \sin jl \right) \qquad (2)$$

where l is the orbital mean anomaly (Folkner et al., 1997). Its derivative

$d\delta\phi/dt = \omega$ provides the rate of rotation. The rotation about the pole ϕ and rotation rate ω, Mars' obliquity ε (the tilt of the spin axis relative to the orbital plane) and its rate $d\varepsilon/dt$, the mean longitude of the node of intersection between the Mars' orbital and equatorial planes ψ_0 and the precession rate $d\psi/dt$, and the rotation constants from Equation (2) are calculated. See Folkner et al. (1997) for more information on determination of Mars' obliquity and mean orbit.

For a specified set of model parameters, considering what we know at present from theory or complementary observations (called the nominal model), MONTE and GINS determine a computed frequency based on the Doppler shift accounting for the known uplink reference frequency and turnaround ratio of the SDST, the motion of both Mars and Earth provided by the DE430 planetary ephemeris (Folkner et al., 2014), Earth orientation parameters provided by JPL's Time and Earth Motion Precision Observation group (for MONTE) and the International Earth Rotation and Reference Systems Service (IERS) Service of Earth Rotation (for GINS), and all of the tropospheric and ionospheric calibrations mentioned in Section 3. The difference between the computed frequency and the actual observed frequency (the residual frequency) is attributed to the difference between the nominal model and the actual Martian spin angle amplitude and spin axis direction. The determination of Mars' rotation and orientation then consists of adjustment to the model parameters in order to match the model predictions with the actual tracking observations. MONTE and GINS solve for new parameter values which will drive residuals to zero mean for all four missions.

As explained above, the current data set is presently too limited to determine new values for the periodic changes in Mars' orientation, and only precession and obliquity rates are estimated together with mean seasonal changes in Mars' rotation and with the lander positions (except for the longitude of Viking). For this paper, the longitude of Viking-1 was held fixed at $-47.95137°$ as in Kuchynka et al. (2014) to define the Mars-fixed coordinate system. In doing so, the precision of the Viking lander longitude replaces the less certain position of the prime meridian defined as the center of Airy-O crater. The longitude and distance from the Martian axis of rotation (cylindrical radius) for Pathfinder, Opportunity, and each medium-gain antenna of InSight were estimated from the Doppler data, with the distance from the equator (z coordinate) determined by comparing the longitude and radius of each antenna with the topography determined by the Mars Observer Laser Altimeter (Le Maistre, 2016).

Fig. 3 shows the residual frequencies for each of the four missions, having been determined according to the above procedure. For Viking-1 (Fig. 3A), the entirety of the observations are solar-plasma dominated, as indicated in Section 3. Thus, residuals are higher than for the subsequent three missions, which is reflected in the higher root-mean square error (RMS). The two shaded regions near solar conjunction are especially affected due to the low SEP angle. Both Pathfinder (Fig. 3B) and Opportunity (Fig. 3C) data were collected at high SEP angles, resulting in low residuals. Opportunity data have low noise, as evidenced by the standard deviation, since the 4 months of data were acquired near Mars opposition and limited by night-time troposphere fluctuation. The InSight (Fig. 3D) data taken shortly after landing were also near Mars opposition with noise similar to that of Opportunity data, but with noise increasing as Mars moved into the daytime sky and then near solar conjunction. Only during solar conjunction (i.e. SEP $<15°$) do the data become solar plasma limited, resulting in higher residuals. In all cases, the residuals have been brought to zero mean as described above.

Table 2 provides updated estimations from GINS of the model parameters described above, along with the conventional Mars mean orbit inclination and longitude of ascending node of 1980 (Konopliv et al., 2006) and the estimated position of the center point between the two InSight antennas. From the combination of lander data, we estimate a precession rate of -7605 ± 3 mas/yr. The results computed with MONTE (-7610 ± 3 mas/yr) and with GINS are within each other's error limits. The difference in these two values is expected from use of slightly different data weighting calibrations at the two institutions as opposed to a difference in the software.

5. Interpretation

The precession rate $d\psi/dt$ is related to the polar moment of inertia C by (e.g., Konopliv et al., 2011)

$$\frac{d\psi}{dt} = -\frac{3}{2}\frac{n_0^2}{C}\frac{1}{\omega}(1-e^2)^{-\frac{3}{2}}J_2\cos(\varepsilon) + \dot{\psi}_g + \dot{\psi}_p \tag{3}$$

where $n_o = 191.408°$/yr is the mean motion of Mars (Konopliv et al., 2011), ω is the computed spin rate (Table 2), $e = 0.09341$ is the orbit eccentricity determined from radio range measurements to spacecraft orbiting Mars (Yoder, 1995), $J_2 = 0.00195660888 \pm 2.82e{-}10$ is the degree-2 unnormalized gravity coefficient estimated from Doppler tracking of spacecraft orbiting Mars (Konopliv et al., 2016), ε is the computed obliquity (Table 2), $\dot{\psi}_g = 6.75$ mas/yr is the geodetic precession (Baland et al., 2020), and $\dot{\psi}_p = -0.77$ mas/yr is the precession resulting from the torque of the other planets as well as from Phobos and Deimos (Baland et al., 2020). The obliquity ε is also varying in time but the changes are very small as shown in Table 2 and are of the second order in Equation (3).

The value of the normalized polar moment of inertia to one sigma is then

$$\frac{C}{Mr_e^2} = 0.363853 \pm 0.000144 \tag{4}$$

where $M = 6.41712 \times 10^{23}$ kg is the mass of Mars (GM = 42,828.4 km³/s², Konopliv et al., 2016) and $r_e = 3396$ km is the equatorial radius derived from the Mars Observer Laser Altimeter (Smith et al., 2001).

By combining the polar moment of inertia C with the accurately known constant part of the degree-2 order-0 gravity field J_2, the mean moment of inertia I of Mars, which is invariant to all deformations lacking a spheroidal component of degree 0, can be determined from (Rochester and Smylie, 1974)

$$\frac{I}{Mr_a^2} = \frac{A+B+C}{3Mr_a^2} = \left(\frac{C}{Mr_e^2} - \frac{2}{3}J_2\right)\frac{r_e^2}{r_a^2} \equiv MOI = 0.363941 \pm 0.000144 \tag{5}$$

where A and B are the two principal equatorial moments of inertia of Mars and $r_a = 3389.5$ km is its mean radius. The error bars associated with C (Eq. (4)) and I (Eq. (5)) have been computed by propagating uncertainties in Equation (3) parameters using a Monte Carlo procedure. Because of the high accuracy of Mars orbital motion (few meters accuracy), n_o, e, and $\dot{\psi}_g$ have been considered well-known as well as $\dot{\psi}_p$. Konopliv et al. (2011) computed normalized MOI as 0.3644, and Konopliv et al. (2016) updated the estimate to 0.3637, as displayed in Fig. 4.

The MOI quantifies the radial mass distribution within the planet. It is mainly determined by the mass of the mantle and crust because the core has a smaller volume and is closer to the center of Mars. To constrain the radius and density of the core from the moment of inertia, prior assumptions about the composition and thermal state of the mantle as well as about the density and thickness of the crust are required. Fig. 4 shows a particular range of interior models that fit the bulk parameters of Mars (e.g., mass and radius) while varying the radius of the core (Rivoldini et al., 2011). The models shown are further characterized by an assumed thickness and density of the crust, composition of the mantle, and mantle temperature profile (case 16, Plesa et al., 2016). The current value and uncertainty of the MOI are indicated. Improvements in the MOI determination narrow the range of possible core radii, but the range is strongly dependent on the assumed crust and mantle structure as is illustrated in the figure, which shows how it is affected by a crust thickness variation of 10 km and by the mantle temperature profile (case 22, Plesa et al., 2016).

6. Conclusions

With the combination of data from InSight and the three previous Mars lander missions, we have estimated a Mars precession rate of -7605 ± 3 mas/yr. This estimate is in close agreement with Kuchynka et al.'s (2014) results from combined lander and orbiter data of -7606.1 ± 3.5 mas/yr. While our solution is significantly different from Kuchynka et al.'s (2014) lander-only estimate of -7619 ± 6.4 mas/yr, it is consistent with the more recent results from Konopliv et al. (2016) with lander tracking only of -7611.4 ± 7.3 mas/yr and with lander and orbiter tracking of -7608.3 ± 2.1 mas/yr (see Fig. 5).

The extra years of coverage from orbiters in addition to landers in Konopliv et al. (2016) gives slightly smaller uncertainty but has not been done here since inter-annual variations in seasonal rotation effects are difficult to quantify. For example, seasonal atmospheric changes related to sublimation and condensation of Mars' polar ice caps cause seasonal changes in the Martian rotation rate observed in the Viking-1 and Mars orbiter Doppler data (Konopliv et al., 2011). Therefore, while seasonal rotation is driven primarily by the Viking-1 data (over ~1 Martian year) for our lander-only estimate, it is also affected by the 2002–2016 time span for Konopliv et al.'s (2016) solution with orbiters. In addition, General Circulation Models of the atmosphere of Mars show that seasonal changes in rotation rate depend significantly on the presence or not of dust storms (Van den Acker et al., 2002), indicating a large interannual variability (at the 10% level). With an additional year of InSight data, the inter-annual variation will be much better characterized.

Our estimate of precession is used to compute the mean MOI as 0.363701 ± 0.000143. This value constrains the radius of the core, dependent on models for the crust and mantle thickness. Additional measurements are needed beyond improvements in precession rate to increase our knowledge about the interior structure. With the addition of a second year of InSight radio Doppler data, the RISE dataset will cover a sufficiently long time span to separate the seasonal rotation rate variations from the nutation of the spin axis direction, allowing for determination of the free-core nutation period and the core moment of inertia. In addition, the continuous sounding of seismic events by the InSight SEIS instrument (Lognonné et al., 2019) will accurately determine the crust thickness and constrain the elastic and thermal properties of the mantle. By combining this knowledge with the accurate moment of inertia from precession, measured tides, and the nutation measurements of RISE, our knowledge about the core radius and density will significantly improve.

CRediT authorship contribution statement

Daniel S. Kahan: Writing – original draft, Data curation. **William M. Folkner:** Conceptualization, Methodology, Supervision, Formal analysis. **Dustin R. Buccino:** Validation, Data curation. **Véronique Dehant:** Methodology. **Sébastien Le Maistre:** Methodology, Formal analysis. **Attilio Rivoldini:** Methodology. **Tim Van Hoolst:** Methodology. **Marie Yseboodt:** Methodology. **J.C. Marty:** Software.

Declaration of competing interest

The authors declare that they have no known competing financial interests or personal relationships that could have appeared to influence the work reported in this paper.

Acknowledgements

Appendix A

Most orbit-determination software such as used here for estimation of Martian rotation assumes that the data points are uncorrelated with time. This is correct for Doppler measurements for which the Earth troposphere fluctuations are the dominant noise; in this case the optimal data weighting is the inverse of the root-mean-square (RMS) of the measurement residuals.

For Doppler data with dominant noise limited by solar plasma, the Doppler measurements are not uncorrelated. The optimum least-squares estimate would use a data weighting matrix that includes the correlated measurement noise. Since the signature of Martian rotation is largely at the time scale of the Martian day, a near-optimal estimate can be derived by treating the measurements as uncorrelated but reducing the data weight by a multiple of the RMS to give the correct power spectral index of the data noise at the diurnal time scale.

For Doppler data with noise dominated by solar plasma fluctuations, the noise power spectral density $S_{s.\,p.}$ has the form

$$S_{s.p.}(f) = h_{s.p.} f^{-2/3} \tag{6}$$

where f is the signal frequency and $h_{s.\,p.}$ is amplitude. For uncorrelated data the noise power spectral density S_w is white (independent of frequency) and has the form

$$S_w(f) = h_w \, f^0 \tag{7}$$

For a given power spectrum S, the variance of the measurement residuals at time interval τ is given by

$$\sigma_{rms^2}(\tau) = \int_0^\infty S(f) \left[\sin\left(\pi f \tau\right) \Big/ \left(\pi f \tau\right) \right]^2 df \tag{8}$$

For the white spectrum this gives

$$\sigma_{rms}^2(\tau) = h_w \, / \, (2\tau) \tag{9}$$

For the solar plasma Doppler spectrum this gives

$$\sigma_{rms}^2(\tau) = h_{s.p.} (\pi\tau)^{-1/3} \, 3.35 \tag{10}$$

From Equations (9) and (10), we see that the white spectrum would underestimate the solar plasma noise at time scales longer than the interval between data points. Assuming that to fit a spectral signature at $f = 1/(T)$, e.g. $T = 88620$ s, the inferred white power spectrum should be scaled up to match the solar power spectrum at that frequency, we define a scaled white power spectrum amplitude by effectively assuming an increase in RMS residuals by a factor F:

$$h'_w = F^2\,\sigma_{rms}^2(\tau)\,2\tau = h_{s.p.}f^{-2/3} \tag{11}$$

with the scale factor F given by

$$F^2 = \frac{\pi^{\frac{1}{3}}}{2 \times 3.35}\left(\frac{T}{\tau}\right)^{2/3} = \left[0.468\left(\frac{T}{\tau}\right)^{1/3}\right]^2 \tag{12}$$

Applying $T = 88620$ s per Martian day and $\tau = 60$-s count time,

$$F = [0.468(88620/60)^{1/3}] = 5.33. \tag{13}$$

Data availability

ASCII versions of the Doppler data for Viking and Pathfinder are in the REDUCED directories at https://pds-geosciences.wustl.edu/missions/mpf/radioscience.html. Opportunity raw tracking data can be found at: https://pds-geosciences.wustl.edu/mer/mer1-m-rss-1-edr-v1/mer1rs_0002/. InSight tracking data are archived at https://pds-geosciences.wustl.edu/missions/insight/rise.htm.

References

Agle, D.C., Brown, D., Wendel, J., 2018. InSight Mission News: Mars New Home 'a Large Sandbox. Retrieved from. https://mars.nasa.gov/news/8395/mars-new-home-a-large-sandbox/?site=insight.

Armstrong, J.W., 1998. Radio wave phase scintillation and precision Doppler tracking of spacecraft. Radio Sci. 33 (6), 1727–1738. https://doi.org/10.1029/98RS02317.

Asmar, S.W., Armstrong, J.W., Iess, L., Tortora, P., 2005. Spacecraft Doppler tracking: noise budget and accuracy achievable in precision radio science observations. Radio Sci. 40 (2) https://doi.org/10.1029/2004RS003101.

Baland, R.-M., Yseboodt, M., Le Maistre, S., Rivoldini, A., Van Hoolst, T., Dehant, V., 2020. The Precession and Nutations of a Rigid Mars: Analytical Developments. Celestial Mechanics and Dynamical Astronomy (submitted for publication.

Bergeot, N., Witasse, O., Le Maistre, S., Blelly, J.L., Kofman, W., Peter, K., Dehant, V., Chevalier, J.M., 2019. MoMo: a new empirical model of the Mars ionospheric total electron content based on Mars Express MARSIS data. A new empirical model of the Mars ionospheric total electron content based on Mars Express MARSIS data. J. Space Weather Sci. 9, A36. https://doi.org/10.1051/swsc/2019035.

Bar-Sever, Y.E., Jacobs, C.S., Keihm, S., Lanyi, G.E., Naudet, C.J., Rosenberger, H.W., Vigue-Rodi, Y., 2007. Atmospheric media calibration for the deep space. Proc. IEEE (95), 2180–2192. https://doi.org/10.1109/JPROC.2007.905181.

Bouquillon, S., 2000. Rotation D'un Corps Rigide. Application a Mars. Ph.D. Thesis. Observatoire de Paris, France, p. 214.

Dehant, V., Le Maistre, S., Baland, R.M., Bergeot, N., Karatekin, Ö., Péters, M.-J., Rivoldini, A., Ruiz Lozano, L., Temel, O., Van Hoolst, T., Yseboodt, M., Mitrovic, M., Kosov, A.S., Valenta, V., Thomassen, L., Karki, S., Al Khalifeh, K., Craeye, C., Gurvits, L.I., Marty, J.-C., Asmar, S., Folkner, W., the LaRa team, 2020. The radio-science LaRa instrument onboard ExoMars 2020 to investigate the rotation and interior of Mars. Planet. Space Sci. 180, 104746. https://doi.org/10.1016/j.pss.2019.104776. Id.

Evans, S., Taber, W., Drain, T., Smith, J., We, H.-C., Guevara, M., Evans, J., 2018. MONTE: the next generation of mission design and navigation software. CEAS Space Journal 10 (1), 79–86. https://doi.org/10.1007/s11214-018-0530-5.

Folkner, W.M., Dehant, V., Le Maistre, S., Yseboodt, M., Rivoldini, A., Van Hoolst, T., Golombek, M.P., 2018. The rotation and interior structure experiment on the InSight mission to Mars. Space Sci. Rev. 214 (5) https://doi.org/10.1007/s11214-018-0530-5.

Folkner, W.M., Williams, J.G., Boggs, D.H., Park, R.S., Kuchynka, P., 2014. The Planetary and Lunar Ephemerides. Interplanetary Network Progress Report, 196.

Folkner, W.M., Yoder, C.F., Yuan, D.-N., Standish, E.M., Preston, R.A., 1997. Interior structure and seasonal mass redistribution of Mars from radio tracking of Mars pathfinder. Science 278 (5344), 1749–1752. https://doi.org/10.1126/science.278.5344.1749.

Folkner, W.M., Iess, L., Anderson, J.D., Asmar, S.W., Buccino, D.R., Durante, D., Feldman, M., Gomez Casajus, L., Gregnanin, M., Milani, A., Parisi, M., Park, R.S., Serra, D., Tommei, G., Tortora, P., Zannoni, M., Bolton, S.J., Connerney, J.E.P., Levin, S.M., 2017. Jupiter gravity field estimated from the first two Juno orbits. Geophys. Res. Lett. 44 (10), 4694–4700. https://doi.org/10.1002/2017GL073140.

Francois, L.M., Walker, J.C.G., Kuhn, W.R., 1990. A numerical simulation of climate changes during the obliquity cycle on Mars. J. Geophys. Res. 95, 14761–14778. https://doi.org/10.1029/jb095ib09p14761.

Golombek, M.P., 1997. The Mars pathfinder mission. J. Geophys. Res. 102 (E2), 3953–3965. https://doi.org/10.1029/96JE02805.

Golombek, M.P., Cook, R.A., Economou, T., Folkner, W.M., Haldemann, A.F., Kallemeyn, P.H., Vaughan, R.M., 1997. Overview of the Mars pathfinder mission and assessment of landing site predictions. Science 278 (5344), 1743–1748. https://doi.org/10.1126/science.278.5344.1743.

Golombek, M.P., Kipp, D., Warner, N., Daubar, I.J., Fergason, R., Kirk, R.L., Banerdt, W.B., 2017. Selection of the InSight landing site. Space Sci. Rev. 211 (1–4), 5–95. https://doi.org/10.1007/s11214-016-0321-9.

Golombek, M., Warner, N.H., Grant, J.A., et al., 2020. Geology of the InSight landing site on Mars. Nat. Commun. 11, 1014. https://doi.org/10.1038/s41467-020-14679-1.

Konopliv, A.S., Yoder, C.F., Standish, E.M., Yuan, D.-N., Sjogren, W.L., 2006. A global solution for the Mars static and seasonal gravity, Mars orientation, Phobos and Deimos masses, and Mars ephemeris. Icarus 182 (1), 23–50. https://doi.org/10.1016/j.icarus.2005.12.025.

Konopliv, A.S., Asmar, S.W., Folkner, W.M., Karatekin, O., Nunes, D.C., Smrekar, S.E., Yoder, C.F., Zuber, M.T., 2011. Mars high resolution gravity fields from MRO, Mars seasonal gravity, and other dynamical parameters. Icarus 211 (1), 401–428. https://doi.org/10.1016/j.icarus.2010.10.004.

Konopliv, A.S., Park, R.S., Folkner, W.M., 2016. An improved JPL Mars gravity field and orientation from Mars orbiter and lander tracking data. Icarus 274, 253–260. https://doi.org/10.1016/j.icarus.2016.02.052.

Kuchynka, P., Folkner, W.M., Konopliv, A.S., Parker, T.J., Park, R.S., Le Maistre, S., Dehant, V., 2014. New constraints on Mars rotation determined from radiometric tracking of the opportunity Mars exploration rover. Icarus 229 (340), 340–347. https://doi.org/10.1016/j.icarus.2013.11.015.

Laskar, J., 1988. Secular Evolution of the solar system over 10 million years. Astron. Astrophys. 198, 341–362.

Le Maistre, S., 2016. InSight coordinates determination from direct-to-Earth radio-tracking and Mars topography model. Planet. Space Sci. 121, 1–9. https://doi.org/10.1016/j.pss.2015.11.003, 2016.

Le Maistre, S., 2020. Martian lander radio-science data calibration for Mars troposphere. Radio Sci. https://doi.org/10.1029/2020RS007155.

Lillis, R.J., Brain, D.A., England, S.L., Withers, P., Fillingim, M.O., Safaeinili, A., 2010. Total electron content in the Mars Ionosphere: temporal studies and dependence on solar EUV flux. Journal of Geophysical Research Space Physics 115 (A11). https://doi.org/10.1029/2010JA015698.

Lodders, K., Fegley, B., 1997. An oxygen isotope model for the composition of Mars. Icarus 126 (2), 373–394. https://doi.org/10.1006/icar.1996.5653.

Lognonné, P., Banerdt, W.B., Giardini, D., et al., 2019. SEIS: insight's seismic experiment for internal structure of Mars. Space Sci. Rev. 215, 12. https://doi.org/10.1007/s11214-018-0574-6.

Mannucci, B.D., Wilson, B.D., Yuan, D.-N., Ho, C.H., Lindqwister, U.J., Runge, T.F., 1998. A global mapping technique for GPS-derived ionospheric. Radio Sci. 33 (3), 565–582. https://doi.org/10.1029/97RS02707.

Marty, J.C., Loyer, S., Perosanz, F., Mercier, F., Bracher, G., Legresy, B., Lemoine, J.M., 2011. GINS: the CNES/GRGS GNSS scientific software. In: Proceedings of the 3rd International Colloquium Scientific and Fundamental Aspects of the Galileo Programme, ESA Proceedings WPP326, 31. Copenhagen, Denmark.

Mohapatra, R.K., Murty, S.V.S., 2003. Precursors of Mars: constraints from nitrogen and oxygen isotopic compositions of Martian meteorites. Meteoritics Planet Sci. 38 (2), 225–241. https://doi.org/10.1111/j.1945-5100.2003.tb00261.x.

Plesa, A.C., Grott, M., Tosi, N., Breuer, D., Spohn, T., Wieczorek, M.A., 2016. How large are present-day heat flux variations across the surface of Mars? J. Geophys. Res. Planets 121 (12), 2386–2403. https://doi.org/10.1002/2016JE005126.

Reasenberg, R.D., King, R.W., 1979. The rotation of Mars. J. Geophys. Res.: Solid Earth 84 (B11), 6231–6240. https://doi.org/10.1029/JB084iB11p06231.

Rivoldini, A., Van Hoolst, T., Verhoeven, O., Mocquet, A., Dehant, V., 2011. Geodesy constraints on the interior structure and composition of Mars. Icarus 213 (2), 451–472. https://doi.org/10.1016/j.icarus.2011.03.024.

Rochester, M.G., Smylie, D.E., 1974. On changes in the trace of the Earth's inertia tensor. JGR 79 (32), 4948–4951.

Sanloup, C., Jambon, A., Gillet, P.A., 1999. Simple chondritic model of Mars. Phys. Earth Planet. In. 112, 43–54. https://doi.org/10.1016/S0031-9201(98)00175-7.

Sears, F.W., Brehme, R.W., 1968. Introduction to the Theory of Relativity. Addison-Wesley, Reading, MA.

Smith, D.E., Zuber, M.T., Frey, H.V., Garvin, J.B., Head, J.W., Muhleman, D.O., Pettengill, G.H., et al., 2001. Mars orbiter laser altimeter: experiment summary after the first year of global mapping of Mars. J. Geophys. Res.: Plan 106 (E10), 23689–23722. https://doi.org/10.1029/2000JE001364.

Soffen, G.A., Snyder, C.W., 1976. The first viking mission to Mars. Science 193 (4255), 759–766. https://doi.org/10.1126/science.193.4255.759.

Squyres, S.W., Arvidson, R.E., Bell III, F.F., Bruckner, J., Cabrol, N.A., Calvin, W., Yen, A., 2004. The Spirit rover's athena science investigation at Gusev crater, Mars. Science 305 (5685), 794–799. https://doi.org/10.1126/science.1100194.

Taylor, G.J., 2013. The bulk composition of Mars. Chem. Erde 73, 401–420. https://doi.org/10.1016/j.chemer.2013.09.006.

Touma, J., Wisdom, J., 1993. The chaotic obliquity of Mars. Science 259, 1294–1297. https://doi.org/10.1126/science.259.5099.1294.

Van den Acker, E., Van Hoolst, T., de Viron, O., Defraigne, P., Dehant, V., Forget, F., Hourdin, F., 2002. Influence of the winds and of the CO2 mass exchange between the atmosphere and the polar ice caps on Mars' orientation parameters. J. Geophys. Res. 107 (E7) https://doi.org/10.1029/2000JE001539, 9-1, CiteID 5055.

Viking Mission to Mars, 1988. Retrieved from NASA Facts: https://mars.nasa.gov/internal_resources/828/.

Ward, W.R., 1974. Climatic variations on Mars: 1. Astronomical theory of insolation. J. Geophys. Res. 79 (24), 3375–3386. https://doi.org/10.1029/JC079i024p03375.

Yoder, C.F., 1995. In: Ahrens, Thomas J. (Ed.), Astrometric and Geodetic Properties of Earth and the Solar System, vol. 1. American Geophysical Union, Washington, DC, p. 88. https://doi.org/10.1029/RF001p0001.

Yoder, C.F., Standish, E.M., 1997. Martian precession and rotation from Viking lander range data. Journal of Geophysical Research, Planets 102 (E2), 4065–4080. https://doi.org/10.1029/96JE03642.

Yseboodt, M., Dehant, V., Peters, M.J., 2017. Signatures of the Martian rotation parameters in the Doppler and range. Planet. Space Sci. 144, 74–88. https://doi.org/10.1016/j.pss.2017.05.008.